Acta Materialia 197 (2020) 253–268

Contents lists available at ScienceDirect

Acta Materialia

journal homepage: www.elsevier.com/locate/actamat

Full length article

Quantification of hydrogen trapping in multiphase steels: Part II – Effect of austenite morphology

Andrej Turk[a,c], Shengda D. Pu[b], David Bombač[e], Pedro E.J. Rivera-Díaz-del-Castillo[d], Enrique I. Galindo-Nava[a,*]

[a] Department of Materials Science and Metallurgy, University of Cambridge, 27 Charles Babbage Road, Cambridge CB3 0FS, United Kingdom
[b] Department of Materials, University of Oxford, Parks Road, Oxford, United Kingdom
[c] OxMet Technologies Ltd, Unit 15, Oxford Business Park, Yarnton, Kidlington, United Kingdom
[d] Department of Engineering, Lancaster University, Gillow Ave, Bailrigg, Lancaster, United Kingdom
[e] Faculty of Natural Sciences and Engineering, University of Ljubljana, Aškerčeva cesta 12, Ljubljana 1000, Slovenia

ARTICLE INFO

Article history:
Received 8 October 2019
Revised 18 June 2020
Accepted 14 July 2020
Available online 17 July 2020

Keywords:
Hydrogen diffusion
Austenite
Interface diffusion
Duplex stainless steel
Hydrogen desorption
Hydrogen permeation

ABSTRACT

We tackle the role of austenite in multiphase steels on hydrogen diffusion systematically for the first time, considering a range of factors such as morphology, interface kinetics and the additional effect of point traps using both experiments and modelling. This follows the findings from part I where we showed that austenite cannot be parametrised and modelled as point traps under the assumption of local equilibrium, unlike grain boundaries and dislocations. To solve this, we introduce a 2D hydrogen diffusion model accounting for the difference in diffusivities and solubilities between the phases. We first revisit the as-quenched martensite permeation results from part I and show that the extremely low H diffusivity there can be partly explained with the new description of austenite but is partly likely due to quench vacancies. We then also look at the H absorption and desorption rates in a duplex steel as a case study using a combination of simulations and experiments. The rates are shown to depend heavily on austenite morphology and the kinetics of H transition from ferrite to austenite and that an energy barrier is likely associated to this transition. We show that H diffusion through the ferrite matrix and austenite islands proceeds at similar rates and the assumption of negligible concentration gradients in ferrite occasionally applied in the literature is a poor approximation. This approach is also applicable to other austenite-containing steels as well as other multiphase alloys.

1. Introduction

Austenite is an important constituent in a number of modern steels, such as (nano)bainitic, quenched-and-partitioned, duplex and TWIP, as well as TRIP and TRIP-assisted steels. It is often designed to be metastable and undergo displacive transformation under applied strain, increasing both the work hardening of the steel as well as its ductility. However, the reliance on displacive transformation for improving mechanical properties leads to inherent problems with hydrogen embrittlement (HE). Upon the transformation of retained austenite (RA), any H is inherited by the resulting martensite in which local stresses are high and is known to be very sensitive to HE [1,2]. In addition, RA acts as a trapping site for H that can slow down the rate of H diffusion in the material significantly [3,4] and can absorb significant amounts of H [3], though not always [5,6]. These effects seem strongly dependent on its volume fraction and morphology but the connection between them and H diffusion has not yet been fully elucidated. Since the morphology of RA is related to its stability and therefore susceptibility to HE, a better understanding of the morphology–diffusion–embrittlement relationship would be beneficial.

This is important even in steels in which austenite is stable, such as duplex and superduplex steels. HE is a significant problem in these steels because they are used in H-rich service environments in oil and gas as well as nuclear industries [7]. Their microstructure generally consists of equal parts of austenite and ferrite. The austenite grains embedded in a ferrite matrix are highly elongated ellipsoids as a result of hot rolling in the range of 1000

---

[*] Corresponding author.

E-mail addresses: at712@cam.ac.uk (A. Turk), shengda.pu@queens.ox.ac.uk (S.D. Pu), david.bombac@ntf.uni-lj.si (D. Bombač), p.rivera1@lancaster.ac.uk (P.E.J. Rivera-Díaz-del-Castillo), eg375@cam.ac.uk (E.I. Galindo-Nava).

https://doi.org/10.1016/j.actamat.2020.07.039

Table 1
Chemical composition of 2205 duplex steel in wt%.

C	Si	Mn	P	S	Ni	Mo	Nb	Cr	Fe
0.017	0.39	1.45	0.018	0.001	5.17	3.28	0.001	22.61	bal.

°C used in the production of these steels [8], and form a highly anisotropic microstructure with a relatively low density of dislocations [9] and secondary phases.

While a number of experimental studies on H diffusion in duplex steels have been published, *e.g.* [10–22], relatively few modelling studies are available [23–29]. H diffusion is characterised by the large solubility difference between ferrite and austenite which leads to diffusion against the concentration gradient from the former to the latter, making the diffusion process at the interface somewhat complex to treat numerically. The second characteristic stems from the anisotropy of microstructure. The morphology of austenite has a significant impact on the rate of diffusion – H diffusivity normal to the elongated direction of austenite grains is much lower than that measured parallel to it [10].

These complexities have been addressed to various degrees by different authors. Early attempts by Owczarek and Zakroczymski assumed the microstructure to be austenite cylinders of varying radii embedded in a ferrite matrix [23,24]. They used analytical solutions for H flux from a cylinder and a plate in 1D to describe H diffusion into/from the austenite and ferrite phase, respectively. Diffusion in ferrite was assumed to take place on a series of pathways of varying lengths, identified by fitting permeation data to the analytical expression for H flux. Sensitivity to microstructure was achieved by using different size distributions and path lengths for austenite and ferrite, respectively. Later authors discarded this approach in favour of solving the diffusion equation numerically in 2D, although a number of them used considerable simplifications, such as disregarding the differences in solubility [25] or both solubility and diffusivity [26]. Only a handful of studies considered both [27–29] and investigated the effect of austenite morphology and connectivity. However, most did not draw a comparison to experimental data and all used simplified microstructures; only a couple of recent studies considered the solubility and diffusivity differences between the two phases and compared modelling results to diffusion experiments [30,31].

Another poorly understood problem is H interaction with the ferrite-austenite interface. Some studies conclude that it is an important trapping site [4,32], although no first-principles studies of the interface exist to back this, despite the fact that other interfaces, *e.g.* ferrite-carbide ones and grain boundaries in ferrite, have received significant attention [33–35]. We argued in part I of the series that interface trapping does not seem significant and that trapping in the RA interior (bulk trapping) can explain experimental observations better, an idea supported by other studies [1,36]. It is also possible that there is an energy barrier associated to the transition of H between the phases, as was shown to be the case for certain grain boundaries in nickel [37]. The presence of such a barrier could retard the rate of H absorption into/desorption from RA grains and make them more effective, albeit slow-acting traps.

Here, H diffusion in mixtures of ferrite and austenite is studied by accounting for the differences in solubility and diffusivity between the two constituent phases in 2D. The effect of austenite morphology on the rate of diffusion is investigated and compared to experimental results. The kinetics of H diffusion from the ferrite into the austenite phase are investigated as well and demonstrated to be a critical factor in the rate of H diffusion in a two-phase microstructure. In addition, the permeation experiments from part I of this series of papers are re-examined and the effect of austenite morphology on the time lag and the steady-state H flux are investigated. This could not be achieved with a simple 1D model used there and so it had to be assumed that austenite films act as point traps for which the assumption of local equilibrium holds. Having an explicit 2D description of austenite morphology provides a physically more accurate picture of the diffusion process and can be used to determine whether these two assumptions are reasonable, thereby helping understand the role of austenite in H behaviour in multiphase steels.

2. Materials and methods

2205 duplex stainless steel of composition shown in Table 1 was received in the form of a rolled plate. Samples 0.5 mm thick, 10 mm wide and 15 mm to 30 mm long were cut normal to the rolling and compression directions (see Fig. 1). These conditions will hence be referred to as ROL and COM, respectively. All samples were given a 1200 grit finish. To make the sample used to measure the H concentration at saturation, one of the COM samples was manually ground to a thickness of 0.1 mm to decrease the time needed for saturation. Additional samples were cut for X-ray diffraction (XRD) and microscopy. They were polished to a 3 μm and a 1 μm finish for XRD and microscopy, respectively. Microscopy samples were then etched electrochemically in a solution of 30% oxalic acid at an applied potential of 3 V for 15–20 s with the exposed surface of roughly 1 cm^2.

The characterisation of the martensitic sample used to study H permeation was described in part I of this series.

2.1. H charging and thermal desorption, SEM and XRD

For more details about the experimental procedures the reader is referred to part I of this series – only new procedures are described here, *e.g.* the procedure for measuring the saturation concentration. For the sample used to measure the saturation concentration the charging solution was changed every two days to keep its chemistry as stable as possible. The charging time of 6.336×10^5 s was chosen based on an estimated effective diffusivity of 10^{-14} m^2 s^{-1}, which was on the far lower end of the range reported for duplex steels [10,23]. The estimated diffusion length during this time was ~80 μm based on the approximate diffusion length, $x = \sqrt{Dt}$. This distance was well above the half-thickness of the sample and the charging time was therefore deemed sufficient for saturation. The purging time for the TDA of the charged sample was only 10 min to minimise H loss.

XRD was used to measure the volume fractions of austenite and ferrite. Samples were given a 3 μm finish, cleaned with ethanol and then placed on a single-crystal Si disk in order to avoid spurious diffraction peaks. A Bruker D8 Advance was used to perform the scan from 38° to 126° 2θ with a step size of 0.025° and a dwell time of 192 s. The Rietveld refinement algorithm in HighScore+ software was used for quantitative phase fraction analysis. In addition, the March/Dollase model was employed as the microstructure was heavily textured.

The samples for optical and scanning electron microscopy (SEM) were polished to a 3 μm finish after which they were electro-etched in a an aqueous solution of 30 wt% oxalic acid under an applied voltage of 2 V for 10–15 s. SEM was performed on

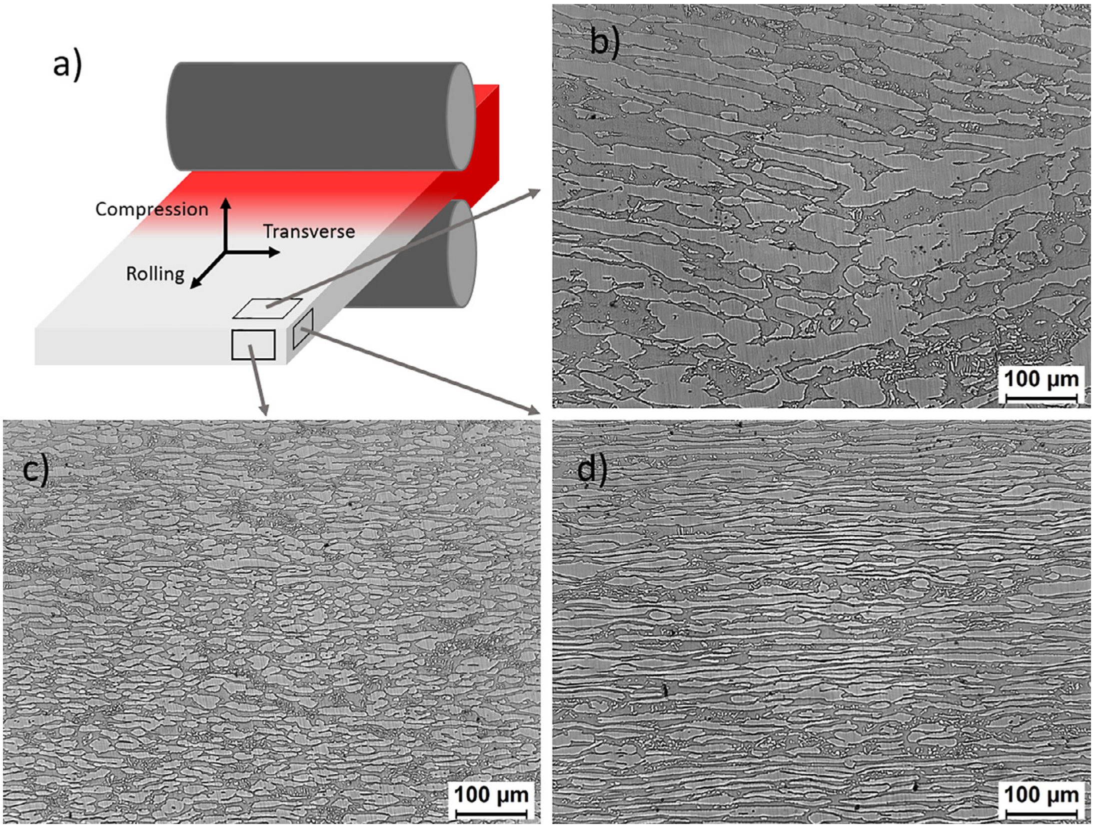

Fig. 1. (a) Schematic of the rolling process and the resulting microstructure normal to the (b) compression direction, (c) rolling direction and d) transverse direction.

the etched samples using an FEI Nova NanoSEM microscope in secondary electron and backscattered electron modes. In both cases the applied voltage was 15 kV – 20 kV, the spot size was 5.5 nm and the working distance 5.1 mm

3. Characterisation results

The microstructure of the material is presented in Fig. 1. The grains of austenite (bright) embedded in a ferrite matrix (dark) are coarse normal to the compression direction and thin and elongated in the transverse direction. The latter was chosen as the input for diffusion simulations as it represents a limiting case in 2D – the diffusion path is by far the most tortuous from the top to the bottom of Fig. 1d. At the same time the micrograph shows the thinnest dimension of the austenite grains which governs their saturation kinetics – if Fig. 1b were used as input instead, the grains would take unrealistically long to saturate with H in simulations.

To obtain input masks for diffusion simulations, an SEM micrograph taken normal to the transverse direction was processed in ImageJ and Matlab. It was first filtered to increase the contrast between the phases and somewhat smoothed prior to binarisation. The binarised image was then processed using different combinations of dilation and erosion steps – care was taken not to alter the ratio of pixels corresponding to ferrite and austenite. The process and its input/output are demonstrated in Fig. 2. The masks in Fig., 2 also show the boundary conditions – the right-hand side was kept at a constant concentration, while the flux was taken to be zero elsewhere due to symmetry considerations. As mentioned, this mask is a representation of the microstructure normal to the transverse direction and therefore shows the longest dimension of the austenite grains. Note also that the distribution of the latter is bimodal. The smaller grains are secondary austenite and given they appear isotropic they likely formed during hot rolling.

The processed mask, while true to the original image, has a somewhat lower fraction of austenite compared to experimental measurements: 55% versus 59 ± 3% determined by XRD. This is largely due to macrosegregation present in the rolled plate – optical microscopy showed that some regions clearly contained more austenite than others. Regardless, given the error of the XRD estimate, the two values are sufficiently close.

The microstructure of the as-quenched martensitic sample used to study H permeation was characterised in part I of this series. It had an average grain size of 25.8 ± 0.4 μm, dislocation density of $(8.6 \pm 1) \times 10^{15}$ m^{-2} and a a retained austenite volume fraction of $(3.5 \pm 0.6) \times 10^{-2}$ (a TEM image showing the austenite films is presented in Section 5). It also contained sparse MX carbonitrides and some cementite, but their effect on H diffusion was estimated to be negligible. This is because their number density is very low (10^{20} m^{-3}), which leads to a low trap density of 5 mol m^{-3} (*e.g.* see Table 3 of part I for comparison against dislocations and grain boundaries). This value was obtained based on a scaling law for H trapping at nano-scale precipitates (~10 nm for carbonitrides) [38].

4. Modelling

The diffusion model shown below was discussed in a previous paper [39]. It incorporates the effect of an arbitrary number of point traps and linearly changing temperature, although here only a single trapping site is considered. Note that while the effect of trapping on defects other than austenite was evaluated (see Fig. 13), it was generally assumed to be negligible for reasons discussed later. The diffusion is now treated in two dimensions, yield-

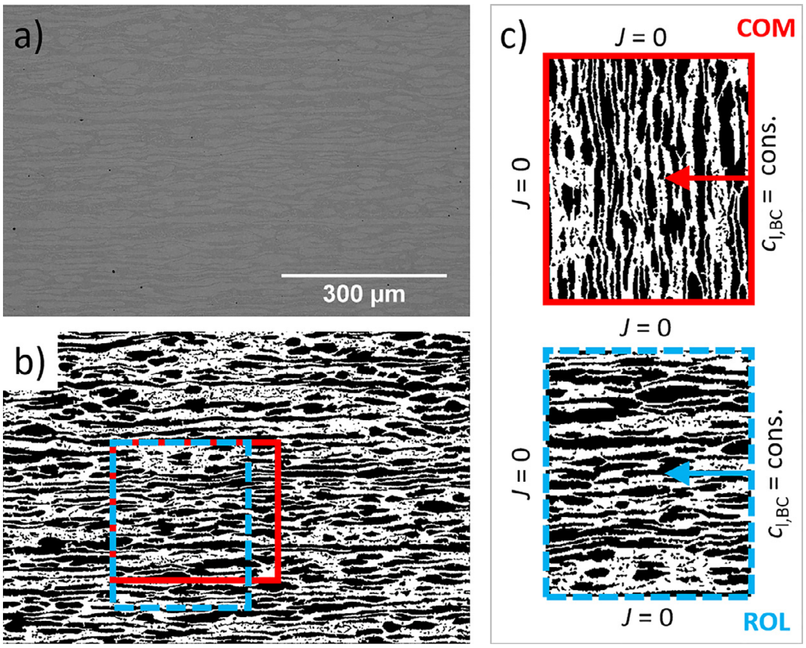

Fig. 2. Illustration of the process for obtaining the input for diffusion simulations. (a) original SEM image, (b) binarised image after processing, (c) the masks used in simulations together with the boundary conditions applied. The masks are tagged ROL (rolling direction) and COM (compression direction) because the direction of H diffusion is *parallel* to them in simulations – see arrows in (c). The dimensions of the masks were 300 µm by 250 µm, with one pixel corresponding to 1 µm. Brighter grains are austenite, while the darker matrix is ferrite.

ing

$$\frac{\partial c_l}{\partial t}=\left(1+\sum_{k=1}^{m}\frac{V_l}{V_{tk}}\frac{K_{tk}}{(K_{tk}+V_l c_l(1-K_{tk}))^2}\right)^{-1}\left(\nabla(J_x+J_y)-\sum_{k=1}^{m}\left(\frac{1}{V_{tk}}\frac{c_l^2V_l^2-c_lV_l}{(K_{tk}+V_lc_l(1-K_{tk}))^2}\frac{K_{tk}\Delta E_{tk}\phi}{RT^2}\right)\right) \tag{1}$$

with

$$J_x=-D_l\frac{\partial c_l}{\partial x};\quad J_y=-D_l\frac{\partial c_l}{\partial y}; \tag{2}$$

where V_l and V_t are molar volumes of interstitial lattice sites and trap sites, respectively. D_l is the diffusivity of H in a defect-free lattice, ΔE_t is the trap binding energy, K_t is its equilibrium constant defined as $K_t=\exp(-\Delta E_t/R/T)$, T is the temperature, ϕ is the heating rate and R is the gas constant. The basis for this model is the notion that the total hydrogen concentration can be split into lattice hydrogen c_l and hydrogen bound to trap c_t and that the two populations are in thermodynamic equilibrium expressed as

$$c_t=\frac{V_l}{V_t}\frac{1}{K_t+V_lc_l(1-K_t)}c_l \tag{3}$$

This formulation works well for diffusion in a single phase but the difference in H solubility must be considered when dealing with a mixture of austenite and ferrite as H may diffuse against the concentration gradient from the latter to the former. One way of incorporating this effect into the model is to recast the H lattice concentration c_l as a fraction of the reference solubility in a given phase, which can be defined at, for example, standard conditions for temperature and pressure. Reference solubility is a function of parameters other than the phase itself, most notably temperature and stress state. An example of this is the built-in mass diffusion model in Abaqus software [40]. This approach has also been considered by a few other authors [41,42], although they did not attempt to correlate their model predictions to real microstructures and experimental data. While the mass diffusion model in Abaqus is able to treat solubility differences it does not incorporate trapping effects which we initially wanted to explore. We therefore decided to write our own custom code.

For Eq. (1), we could use the same approach implemented in Abaqus to treat the solubility difference but this would result in taking additional derivatives on the right-hand side due to spatially varying solubility. This approach introduces some difficulties when implemented in a simple explicit finite difference scheme used here. The stability criterion becomes dependent on the ratio of solubilities between the phases present – because this ratio can be in the range of 10^3 at the interface between austenite and ferrite, the scheme becomes prohibitively slow for diffusion calculations.

We therefore opted for another method instead. The interface between ferrite and austenite can be treated separately and an appropriate definition of local H flux can be found by recognising that in a closed two-phase ferrite-austenite system with H, the ratio of H concentrations in both phases can be approximated with the ratio of H solubilites. Unlike carbon segregation at elevated temperatures where the volume fractions of ferrite and austenite may change to reach thermodynamic equilibrium we are only interested in H at room temperature. The volume fractions of the two phases therefore remain constant because any phase transformation is kinetically suppressed; H however, due to its high diffusivity, redistributes easily. This model effectively treats austenite as a bulk trapping site and assumes no trapping at the interface.

4.1. Ferrite-austenite interface

The condition at the interface has received little attention in studies dealing with diffusion of mixtures of austenite and ferrite, even though it is expected to be an important factor. Two approaches used in this work are explained and compared below.

One way of obtaining the hydrogen flux at the interface is by treating it as an atomic bilayer of ferrite (subscript α) and austenite (subscriptγ) [43,44]. The interface flux J_i between the two can

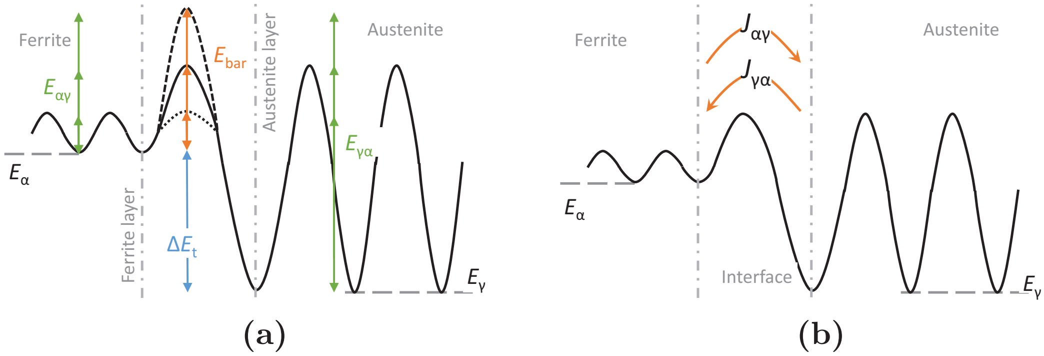

Fig. 3. (a) Illustration of the energy landscape at the α-γ interface in the atomic bilayer model. Stacked arrows indicate the varying magnitude of E_{bar} and its relationship to $E_{\alpha\gamma}$ and $E_{\gamma\alpha}$. At the interface, the dotted line is the energy barrier equal to the activation energy for diffusion in ferrite, while the full one corresponds to that of austenite minus the segregation energy ΔE_{t}. The dashed line indicates some excess energy barrier. (b) Illustration of the H fluxes from α to γ and *vice versa*.

be defined as

$$J_{\mathrm{i}} = c'_{\mathrm{l},\alpha}(1-\theta_{\mathrm{l},\gamma})\Gamma_{\alpha\gamma} - c'_{\mathrm{l},\gamma}(1-\theta_{\mathrm{l},\alpha})\Gamma_{\gamma\alpha};$$

$$\Gamma_{\alpha\gamma} = Z\nu_0 \exp\left(-\frac{E_{\alpha\gamma}}{RT}\right) = Z\nu_0 \exp\left(-\frac{E_{\mathrm{bar}}}{RT}\right)$$

$$\Gamma_{\gamma\alpha} = Z\nu_0 \exp\left(-\frac{E_{\gamma\alpha}}{RT}\right) = Z\nu_0 \exp\left(-\frac{E_{\mathrm{bar}}+\Delta E_{\mathrm{t}}}{RT}\right) \tag{4}$$

where $\Gamma_{\alpha\gamma}$ and $\Gamma_{\gamma\alpha}$ are the fractions of successful jump attempts per unit time from α-Fe to γ-Fe and from γ-Fe to α-Fe, respectively. $E_{\alpha\gamma}$ and $E_{\gamma\alpha}$ are the corresponding energy barriers, illustrated in Fig. 3. They can be expressed as the energy difference between α-Fe and γ-Fe – which is equivalent to trapping energy ΔE_{t} from the concept of trapping – and the energy barrier, E_{bar}. θ_{l} still stands for lattice occupancy and the additional Greek subscripts stand for the phase the layer belongs to. c'_{l} is the planar concentration of H on either side of the bilayer and can be approximated as the product of the lattice concentration c_{l} and the Burgers vector b, which roughly corresponds to the thickness of the plane. At thermodynamic equilibrium, J_{i} is zero and Eq. (4) collapses into the expression for local equilibrium (Eq. (3)).

Next, the jump kinetics may be evaluated. The energy difference between the two phases, *i.e.* the difference between the E_γ and E_α in Fig. 3a, is on the order of 20 kJ mol^{-1} [45], and the activation energies for ferrite and austenite are 8 kJ mol^{-1} and 55 kJ mol^{-1}, respectively. Note that the activation energy refers to lattice diffusion – it is the energy barrier between normal interstitial sites in ferrite and in austenite. If the interface is assumed not to have any additional energy barriers, then $E_{\alpha\gamma}$ and $E_{\gamma\alpha}$ are between 8–35 kJ mol^{-1} and 28–55 kJ mol^{-1}, respectively, depending on whether the energy barrier at the interface is assumed to be that of austenite (solid line) or that of ferrite (dotted line) (see Fig. 3). The jump rate ν_0 has been reported to in the range of 10^{12} s^{-1} [46]. Using these values in a diffusion simulation reveals that a near-equilibrium condition at the interface is established in minutes, implying that, initially, the interface flux is significantly larger than the flux in the austenite region close to the interface despite the large concentration gradients there.

Assuming that there is no additional energy barrier for the transition from α-Fe to γ-Fe, a simpler approximation can therefore be taken for the interface flux. At equilibrium the net interface flux is zero, otherwise the flux will be driven by the gradient in the chemical potential between the phases. For dilute solutions of H, it can be assumed that flux is driven by the concentration rather than the chemical potential gradient. Since the ratio of H concentrations on both sides of the interface will be the same as the solubility ratio[1], the concentration difference between both sides can therefore be obtained by dividing the concentration in austenite by its solubility ratio relative to ferrite, leading to

$$J_{\mathrm{i}} = -\frac{D_{\mathrm{l}}}{\delta x}\left(c_{\mathrm{l},\alpha} - \frac{c_{\mathrm{l},\gamma}}{s_{\mathrm{r}}}\right) \tag{5}$$

where δx is the distance between α-Fe and γ-Fe plane and s_{r} is the ratio of H solubilities in austenite (S_γ) and ferrite (S_α)

$$s_{\mathrm{r}} = \frac{S_\gamma}{S_\alpha} \tag{6}$$

In Eq. (5) the value of δx was approximated with the size of the discretisation step, which is significantly larger than the interface width. Furthermore, the value of D_{l} at the interface is not defined, but barring the presence of an energy barrier, it should lie between the values for pure austenite and pure ferrite. Two cases were tested, one in which the value of D_{l} was a linear average of the two and one in which it was defined as the geometric average $D_{\mathrm{l}} = \sqrt{D_\alpha D_\gamma}$ of the two limiting values. A simple 1D simulation was then run on a domain 30 µm in length, half of which consisted of ferrite while the other half consisted of austenite. A constant-concentration boundary condition was used at the ferrite side and a zero-flux condition at the austenite side to simulate the dependence of the absorption rate versus the value of D_{l}. The results were compared to a more rigorously defined interface condition for diffusion in media with different solubilities and diffusivities derived by Crank [47], also used by Enomoto [28]. It was found that defining the interface D_{l} value as a linear average overestimated the H absorption rate resulted in a difference of 40% relative to Crank's condition. Defining it as a geometric average yielded a relative difference of –20% instead, both for a simulation time of 5000 s. Differences, however, decreased with longer charging time. The results are shown in Fig. 4. Unfortunately, Crank's condition is challenging to implement in 2D and is poorly parallelisable because it involves the use of ghost nodes around all interfaces. Therefore, Eq. (5) using a linear average of ferrite and austenite diffusivities was chosen as the condition representative of an interface without an energy barrier due to its faster convergence to Crank's solution relative to using a geometric average of diffusivities. The absorption rate is initially overestimated, which is expected to lead to an overprediction of the H absorption rate at shorter times for full-scale simulations. However, this error is expected to gradually become sufficiently small over time.

---

[1] If a block of ferrite and a block of austenite dissolve 1 mol m^{-3} and 1000 mol m^{-3} in equilibrium with a H_2 atmosphere of 1 bar at room temperature, respectively, then, if the blocks were joined together, their H concentrations would also be in equilibrium with each other.

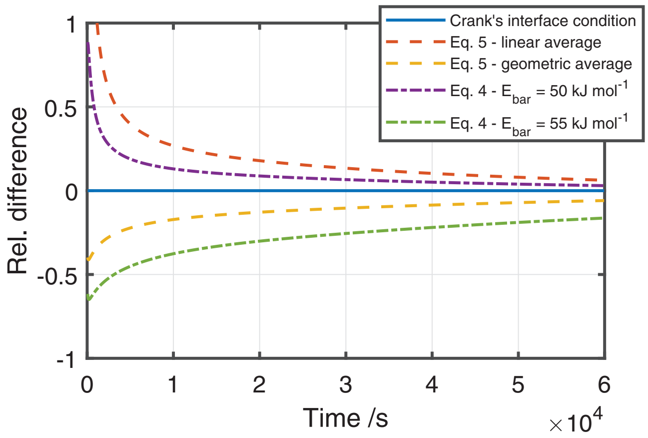

Fig. 4. Difference in H content versus time relative to the interface condition by Crank [47], defined for an interface without an energy barrier or trapping effects. For the interafce condition using Eq. (5), using a geometric average introduces a smaller error initially but converges much slower than using a linear average. For the interface condition using Eq. (4), the energy barrier needs to exceed some 50 kJ mol^{-1} in order to achieve absorption slower than in the barrier-free case.

Fig. 4 also displays the effect of choosing Eq. (4) as the interface condition. Depending on the energy barrier, it can yield higher or lower absorption rates relative to Crank's condition, where the critical value for this transition is between 50 kJ mol^{-1} and 55 kJ mol^{-1}. The results show that the definition of the boundary condition at the interface is far from trivial and can have a large impact on the predicted absorption rates.

4.2. Implementation and parameters

The implementation of the diffusion model in Fortran was performed in two dimensions using an explicit finite difference scheme. In the first step, the flux values in x and y directions were calculated for all grid points using Eq. (2). To treat the interface between the ferrite and austenite the relevant grid points were identified using masks and the flux in x and y directions was defined using either Eq. (4) or (5). In the second step the mass conservation law (Eq. (1)) was applied to update the lattice concentration values on the entire grid. It was found that the size of the grid severely affected the length of the simulation even with relatively small grids. The code was therefore parallelised for GPU execution using OpenACC directives for Fortran – the resulting implementation ran significantly faster on the GeForce Titan Black compared to the implementation on the Intel i7-7700 processor for mesh sizes larger than ~150 by 150 grid points.

Even with parallelisation, the limitations of the explicit finite difference scheme were readily apparent. The stability criterion enforced a small time step for spatial discretisations below ~1 µm, imposing a limit on the smallest resolvable microstructural feature except for the smallest of grids. In order to simulate H absorption in the duplex samples, however, a domain 250 µm in thickness and nearly the same in length was required for an accurate representation of the microstructure, limiting the timescale simulated.

Default simulation parameters are listed in Table 2. Note that trapping, even though explored, was largely assumed to be negligible. This is because of the low defect density in the samples, resulting from the lack of precipitates, relatively large grains and a low dislocation density. Dislocation measurements on duplex steels have shown that the values in hot-rolled plates with a processing history similar to the material used here were on the order of 10^{12} m^{-2} [9]. They should therefore have a negligible impact on the rate of H absorption as demonstrated in part I of this series. The choice of D_α is pertinent to this discussion – the value chosen here was based on high-temperature gas permeation data on a ferritic stainless steel of a similar composition where trapping was assumed to be negligible [48]. The same authors also report a different fit to room-temperature data where trapping effects were significant, resulting in a D_α value an order of magnitude lower. We chose the former because in the permeation experiments used to obtain the data, the boundary condition $c_{l,BC}$ was significantly lower than here and trapping effects are particularly noticeable when $c_{l,BC}$ is low. Indeed, other authors who used very high charging currents in permeation experiments detected diffusivities in the range of 10^{-10} m^2 s^{-1} at room temperature for a similar annealed ferritic stainless steel [49]. However, note that this value is still about two orders of magnitude lower than in pure α-Fe and is likely due to heavy alloying with Cr, Mo and Ni which alters the average energy barrier for H jumps between interstitial lattice sites. Another parameter to mention is Z which denotes the number of neighbouring interstitial sites for a H atom at the α-γ interface contributing to H flux. In austenite, H generally only occupies octahedral sites, while in ferrite and BCC martensite it occupies tetrahedral ones [45]. Of the 12 nearest neighbours of an octahedral interstitial site in austenite, 4 lie on the GB plane and do not contribute to H flux across the boundary, leaving 8 available sites. In ferrite, H occupies tetrahedral sites which have 4 tetrahedral nearest neighbours, none of which lie in the GB plane. Z is then taken as the average of the two taking a simplified view of the GB as the average of the two phases.

5. Results and discussion

5.1. Retained austenite and diffusion in martensite

It is first worthwhile to re-examine some of the experimental results from part I of this series. There, H diffusion properties of three different conditions of martensite were studied using permeation and thermal desorption experiments and it was found that a small amount of RA (3.5×10^{-2}) in the as-quenched condition decreased the effective diffusivity by an order of magnitude relative to the tempered sample with the same dislocation density, grain

Table 2
Parameters used in H absorption simulations in duplex steel.

Parameter	Value	Ref.	Comment
$c_{l,BC,\gamma}$	346.7 wppm	-	discussed in the paper
ΔE_t	19.17 kJ mol^{-1}	[50,51]	from H solubilities of γ-Fe and α -Fe at standard conditions
s_r	2.16 $\times$ 10^3	[50,51]	from H solubilities of γ-Fe and α-Fe at standard conditions
E_{bar}	varies	[50,51]	discussed above
D_α	3.87×10^{-10} m^2 s^{-1}	[48]	
D_γ	$5.4 \times 10^{-7} \exp(-53.9/RT)$	[52]	activation energy in kJ mol^{-1}
ν_0	10^{12} s^{-1}	[46]	
Z	6		average of tetrahedral (4 neighbours, α - Fe) and octahedral (8 neighbours, γ - Fe)
N_l	2.0 $\times 10^5$ mol m^{-3}	[53]	
T	300 K	-	laboratory conditions

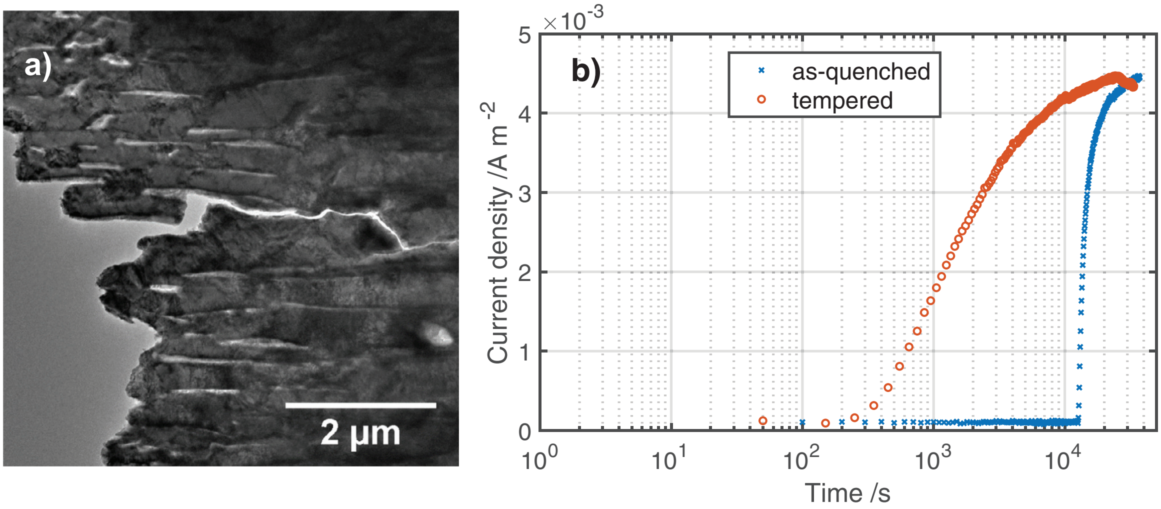

Fig. 5. (a) TEM image of the as-quenched microstructure showing austenite films. (b) Permeation curves for as-quenched and tempered martensite.

size and carbide distribution. While RA was treated as a point trap assuming local equilibrium, we showed that this assumption was not physically sound and that austenite should be modelled explicitly. Fig. 5a is a TEM image of the as-quenched microstructure showing austenite films of width ~10 nm – 20 nm and b) the permeation curves for the as-quenched and tempered (300 °C) samples showing significant differences in the time lag between each condition.

As austenite forms films on lath interfaces, it should not only act as a H sink but also as a morphological obstacle to diffusion. We can therefore imagine two limiting scenarios – one in which austenite films are arranged normal to the direction of diffusion, leading to a more tortuous diffusion path both in the transient and steady-state regimes, along with austenite acting as a sink in the former. The other limiting scenario is one in which austenite films are arranged parallel to the direction of diffusion – here the transient regime will be heavily affected by H trapping but the steady-state regime should only be affected by the volume fraction of austenite which is relatively small. Of course, the real morphology of RA is generally more complex but can be assumed to lie between these two limits.

With this in mind, H permeation through simplified input microstructures containing either no austenite films, films oriented normal to the diffusion direction or films parallel to it and finally blocky RA was simulated. The model parameters are listed in Table 2 and the definition of H flux at the austenite-ferrite interface was taken from Eq. (5). The total thickness of the permeation domain was 741 µm and representative input microstructures are shown in Fig. 6 – dispersed austenite consists of small austenite islands uniformly dispersed in the matrix. In all cases where austenite is present its volume fraction is ~3.5×10^{-2} to reflect the experimentally measured volume fraction. The morphology of austenite chosen here was somewhat arbitrary due to the lack of sufficient experimental data but representative of the thin and discontinuous arrangement of interlath austenite films generally observed in martensitic steels, as shown in Fig. 3 in Part I. The size of the blocky austenite islands was ~30 µm, whereas the austenite films were 75 µm long and 9 µm wide, 45 µm long and 9 µm wide and 75 µm long and 3 µm wide in the case of films normal to the H diffusion path, parallel films and thin parallel films, respectively. The dispersed austenite films were 1 µm in size. The flux was normalised over the height of each grid to eliminate the effect of it varying as a result of changing the austenite morphology.

The resulting permeation transients are shown in Fig. 7a. Since the steady-state flux scales with the product of H diffusivity and solubility, pure ferrite has the highest flux. At room temperature, H solubility in austenite is ~10^3 times higher than in ferrite, while diffusivity is ~10^6 times lower. The steady-state flux is therefore around ~10^3 times lower in pure austenite compared to pure ferrite. Microstructures containing both phases are expected to lie between these two limiting cases. Indeed, all microstructures with austenite show a reduction in the time lag and steady-state flux relative to pure ferrite, with austenite films normal to the direction of diffusion having the largest impact. The variation in steady state flux with austenite morphology is because grains of austenite embedded in ferrite act as a sort of diffusion obstacle whose effect

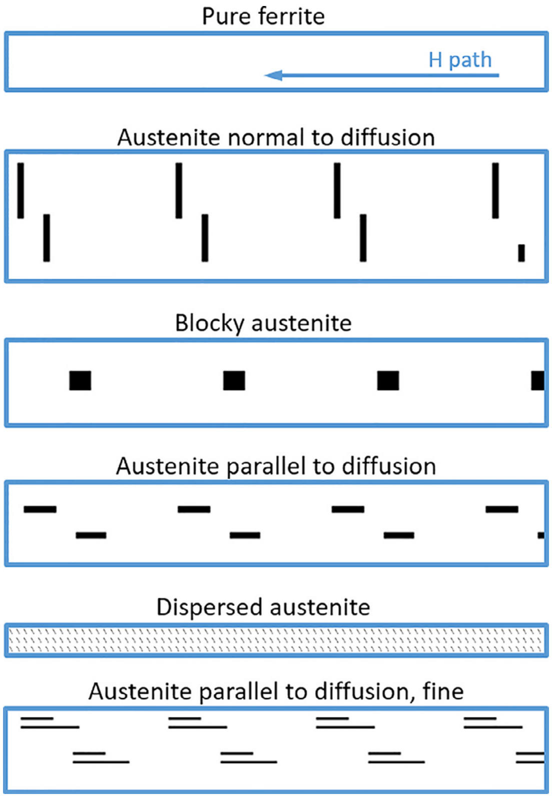

Fig. 6. Schematic input microstructures for H permeation simulations in the presence of austenite (in black). The arrow indicates the general direction of H flux which is tortuous in the presence of austenite – more so when the islands are aligned normal to the diffusion direction.

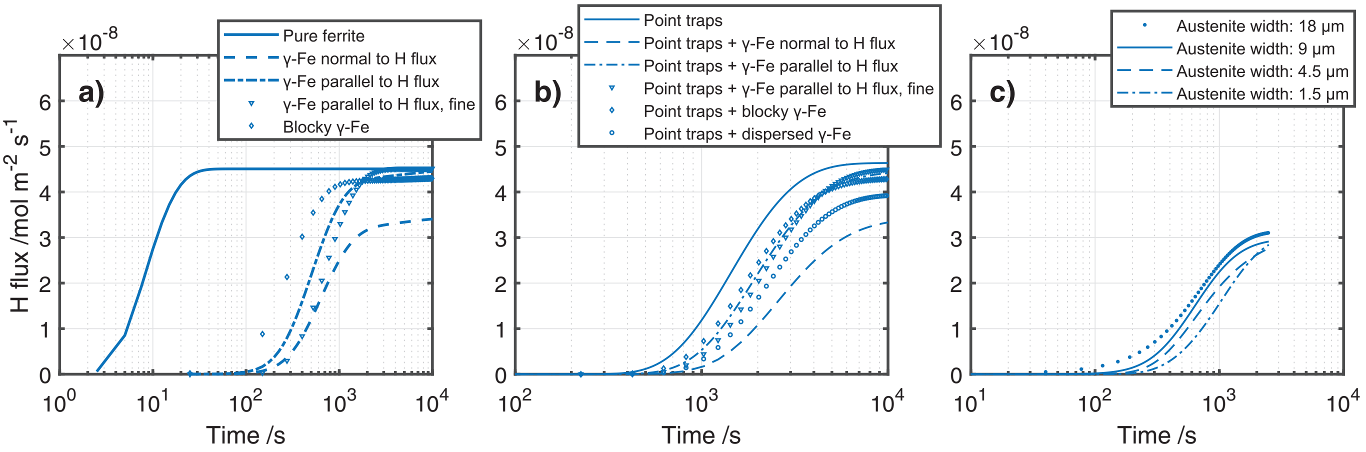

Fig. 7. (a) Permeation transients of microstructures shown in Fig. 6. Austenite significantly decreases both the time lag as well as the steady-state flux (see inset on top right for a comparison with pure ferrite). (b) Experimental transient of as-quenched martensite and comparison of simulation results using various austenite morphologies. The more finely dispersed the austenite the more pronounced the trapping effect. (c) Effect of refining the austenite island size along with the discretisation step. Diminishing size results in a notable increase in time lag.

Table 3
Parameters used in H permeation simulations on martensite.

Parameter	Value
$c_{l,BC,\gamma}$	3.7×10^{-3} mol m^{-3}
ΔE_{dis}	20 kJ mol^{-1}
ΔE_{GB}	30 kJ mol^{-1}
N_{dis}	8.6×10^{3} mol m^{-3}
N_{GB}	56 mol m^{-3}
D_{α}	8.97×10^{-9} m^{2} s^{-1}
N_{l}	2.0×10^{5} mol m^{-3}
T	300 K

depends on the size and alignment of the austenite islands with respect to the direction of H flow.

A few conclusions can be drawn from this simulation. First, if austenite films in martensite are not too elongated (i.e. do not completely envelop laths and/or are discontinuous) they do not obstruct the H diffusion path significantly. In this case, the steady-state H flux may only be minimally affected and may lie within the error of the experiment. If that is indeed the case it is very likely that the time lag in the as-quenched martensite sample in part I is in large part due to trapping in austenite. To corroborate this, a ratio can be estimated between the experimental time lag (time to reach 63% of the steady state current [54]) shown in Fig. 5b for the as-quenched (~15,000 s) and tempered (~1500 s) conditions giving ~10; the same estimate considering our simulations for austenite-containing ferrite, where the time lag is 300 s – 750 s, and 10 s for pure ferrite, gives a ratio in the range of 30–75. For simplified conditions the predicted effect austenite has in H diffusion in ferrite is roughly of the same order of magnitude than that measured experimentally. A more complex case is explored next.

We also ran a permeation simulation more representative of the as-quenched sample from part I, accounting both for point traps as well as austenite. The simulation parameters were taken from part I and are listed in Table 3. Those not listed are the same as in Table 2. Different austenite morphologies from Fig. 6 and a volume fraction of 3.5×10^{-2} were used. The results are shown in Fig. 7b – the presence of austenite significantly increases the time lag and somewhat decreases the steady-state flux. The combined effect of point traps and austenite underestimates the experimentally measured time lag. However, it is important to note that the smallest austenite feature used was on the order of 3 μm, while the films of retained austenite in martensite are only a few nanometres thick (~10 nm - 20 nm), a difference of several orders of magnitude. Since it can be seen that time lag increases with the decreasing size of austenite features (compare blocky and thin films), further reduction in their size is eventually expected to result in a permeation transient more similar to the one observed in experiments. Fig. 7c illustrates this effect. Austenite islands normal to diffusion direction in ferrite were chosen as an example; ferrite was without point traps to isolate the effect of decreasing austenite island size on time lag. As the width of austenite islands decreases from 18 μm to 1.5 μm, the time lag increases from 767 s to 1287 s. Further refinement was not possible due to numerical constraints, but the time lag was extrapolated by fitting the results to a power–law function. The time lag was taken when the flux is ~2×10^{-8} mol m^{-2} s^{-1} s^{-1} (~63% of the steady state current), giving 767 s, 845 s, 1060 s and 1287 s for austenite widths of 18 μm, 9 μm, 4.5 μm and 1.5 μm, respectively; these values were fitted to the function $t = 1418w^{-0.22}$ s, where t and w are time lag and austenite width, respectively, with $r^2 = 0.98$. This formula predicts that austenite islands ~10 nm across cause a time lag on the order of 3905 s. Adding the effect of point traps to the total time lag is then in the range of 5900 s. The combined effect still falls somewhat short of the observed time lag in as-quenched martensite. This indicates that an appreciable effect may be due to quench vacancies as mentioned in part I.

Another feature to note is that the flux rise in Fig. 7a and b is shallower than experimentally observed in the as-quenched sample – this is partly a morphological effect. A finer austenite dispersion leads to a larger time lag as it decreases the time needed for the saturation of the islands [27]. This is apparent from the comparison of the permeation transients of blocky RA and elongated RA aligned parallel to H flux in Fig. 7a – the blocky islands take a longer time to saturate and lead to a faster rise in permeation flux but diffusion also needs a longer time to reach steady state. However, having identified that quench vacancies likely play some role, their presence would also help explain the steep flux rise in as-quenched martensite since this is characteristic of strong point traps as identified in Part I.

5.2. Discussion

It is worth mentioning that the intention in this section is to assess the influence of fine austenite films dispersed within a martensitic matrix on H diffusion, but not to actually reproduce in detail the experimental permeation curves in Fig. 5 b.

The microstructure of martensite is very complex and there is no clear understanding how retained austenite within it is distributed. Martensite is hierarchically structured with a high density of high-angle grain boundaries, 1 μm to 30 μm in size, and each subgrain has a fine distribution of (low-angle) laths, some ~250 nm wide; austenite films are located at the lath boundaries but they may not be present on each one or cover the boundaries entirely. As such, it would be helpful to simulate permeation using nanometre-sized films, representing austenite morphology more closely mimicking that of as-quenched martensite. Unfortunately, this is computationally infeasible: assuming the average thickness of the austenite films is ~10 nm and their spacing is ~250 nm, at least 741 μm /260 nm ≈ 2850 austenite islands per unit height are needed in the simulation, requiring a very large mesh. We would next have to consider that austenite films have a different orientation at different grains/subgrains and that they may not be present on every boundary. In addition, with an explicit finite-difference scheme used in this work and a *dx* on the order or a few nanometres, diffusion times on the order of a few microseconds at best could be achieved due to the constraint on the maximum time step. A better numerical approach would require a specialised study, possibly using an effective-medium approach similar to those used for the simulation of diffusion-reaction processes in porous media [55]. Nonetheless, since we were able to show in Fig. 7a and 7 c that, for the simple case of pure ferrite, fine islands of austenite indeed increase the permeation time lag by an order of magnitude, the present model should be able to capture such effects in martensite if more detailed information of the austenite morphology is available. The morphology in part I should ideally be characterised by a tomographic technique in order to fully quantify the effect of austenite on the time lag. However, as we have found no reported instances of the 3D characterisation of retained austenite at this length scale in the literature, we conclude that this may be outside of the reach of current experimental techniques. Finally, we should remark that quench vacancies are likely to have an appreciable impact on the observed time lag in as-quenched martensite. This is a poorly understood topic that has significant implications for H diffusion and would be worthwhile quantifying in the future.

The permeation simulations presented also indicate that the presence of RA can decrease *both* the effective diffusivity, as well as the steady-state permeation current. Previous studies on the effect of austenite on permeation curves are in line with this observation. Kim *et al.* [56] studied a ferritic and a TRIP steel with similar compositions, where different volume fractions of austenite in the TRIP steel were achieved with deformation. Just like our simulations show, the presence of austenite both increased the time lag as well as decreased the steady-state H permeation current. Similarly, Lan *et al.* [57] used H permeation on bainitic steel weldments exhibiting different volume fractions of what they termed the martensite-austenite constituent. The permeation time lag increased and steady state current decreased with increasing martensite-austenite content. However, our simulations also show that the effect of RA strongly depends on its morphology. If the effective surface area of RA per unit volume is large, its volume fraction low and its morphology such that it does not appreciably obstruct the H diffusion path, the effective diffusivity is significantly reduced, but the steady-state flux may not change appreciably. Conversely, if the morphology does obstruct the H diffusion path, both the steady-state flux and the effective diffusivity change. This has implications for the analysis of experimental permeation data in steels where the variation in steady-state flux between different microstructural conditions is frequently not reported or analysed despite the fact that it may contain information on austenite morphology.

The work presented in this series enables the modelling of H diffusion in martensite and ferrite accounting for the trapping effects of a number of distinct defects, which has, to our knowledge, not been reported before. By knowing the defect density and, when austenite is present, austenite morphology, it is possible to model H diffusion without prior parameter calibration. Moreover, the inaccuracies in modelling retained austenite in martensite seem to be mostly due to a lack of more accurate input morphology, as well as its distribution within the hierarchical structure of lath martensite, and the numerical constraints of the scheme used, both of which can be improved in the future. The current implementation is better suited to microstructures with coarser austenite features whose morphology is understood well, such as those in duplex steel. To corroborate this, the latter is explored next.

5.3. Diffusion in duplex steels

First, the case of ferrite-austenite boundary condition based on Eq. (5) was modelled using as input the masks and boundary conditions in Fig. 2. The constant-concentration boundary condition was calibrated using the experimentally obtained saturation concentration. Virtually all H in the saturated sample can be assumed to reside in austenite, due its large H solubility. Dividing the saturation concentration by the volume fraction of austenite in the steel yielded a H concentration of 346.7 wppm in the austenite phase. The boundary condition for ferrite was obtained by simply multiplying this value by the solubility ratio s_r. The results of the simulations of COM and ROL samples are shown in Figs. 8 and 9, respectively. H penetrates only a short distance into the COM microstructure in contrast with the ROL one after 6×10^4 s.

The simulated rate of H absorption from the model was then compared to experimental values measured with thermal desorption analysis. The standard error was measured directly. However, in a previous study of the effect of deformation on the H absorption of the same material, the charging procedure was shown to produce a standard relative error of ±7%. Since the error was based on a set of measurements comparing as-received to cold-worked material, most of it is likely coming from the microstructural changes due to trapping and very little from the charging procedure itself [22]. The results of the model and the experimental data are shown in Fig. 10. It is clear that H absorption is considerably slower in COM samples, that is normal to the largest facet of the austenitic grains, in simulations as well as experiments. In both cases, the charging times were too short to reach the saturation value of 208 wppm. However, the simulations suggest much more rapid absorption kinetics compared to the experiments. This was unexpected, particularly in the COM sample, where the geometrical considerations discussed before should result in an underestimate of the rate of H absorption. If anything, simulating the problem in 3D would result in even higher absorption rates given that the austenite grains are less elongated in the in-plane direction which would provide a short-cut for H diffusion, if taken into account. Assuming the absence of strong/dense traps which could slow down H absorption, the only explanation for this observation is that H diffusion into austenite grains is limited by a significant energy barrier associated to the transition of H from ferrite into austenite.

Note that H penetration into the ferrite region, even in the ROL case (Fig. 9, bottom row), is very slow. Significantly slower, in fact, than in single phase ferrite, in which the characteristic diffusion length from $x = \sqrt{D_\alpha t}$ is on the order of 1.7 mm after a charging time of 7200 s. At this time, a ferrite sample 0.5 mm thick would have long been saturated with H. From Fig. 9, however, it is clear that in the duplex steel the ferrite matrix is far from saturation, despite the fact that there is little tortuosity associated to H diffusion in ferrite as the austenite grains are oriented parallel to the diffusion direction, forming mostly straight ferrite channels. The continual absorption of H into the austenite phase therefore

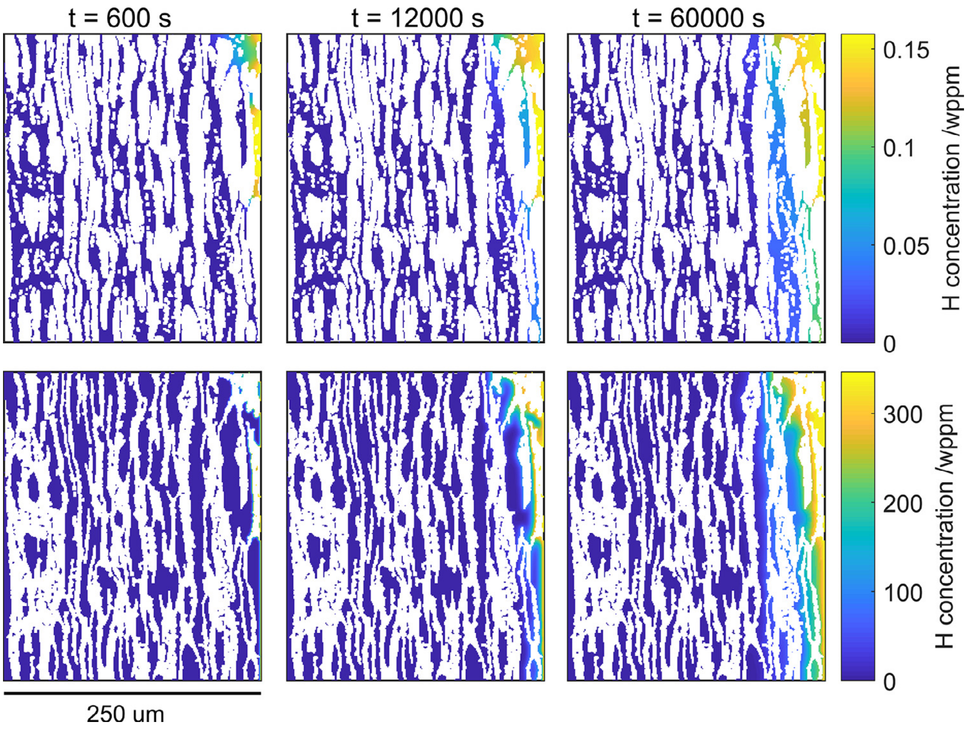

Fig. 8. Maps of H concentration in ferrite (top row) and austenite (bottom row) in the simulated COM sample at different times. Diffusion direction is from right to left.

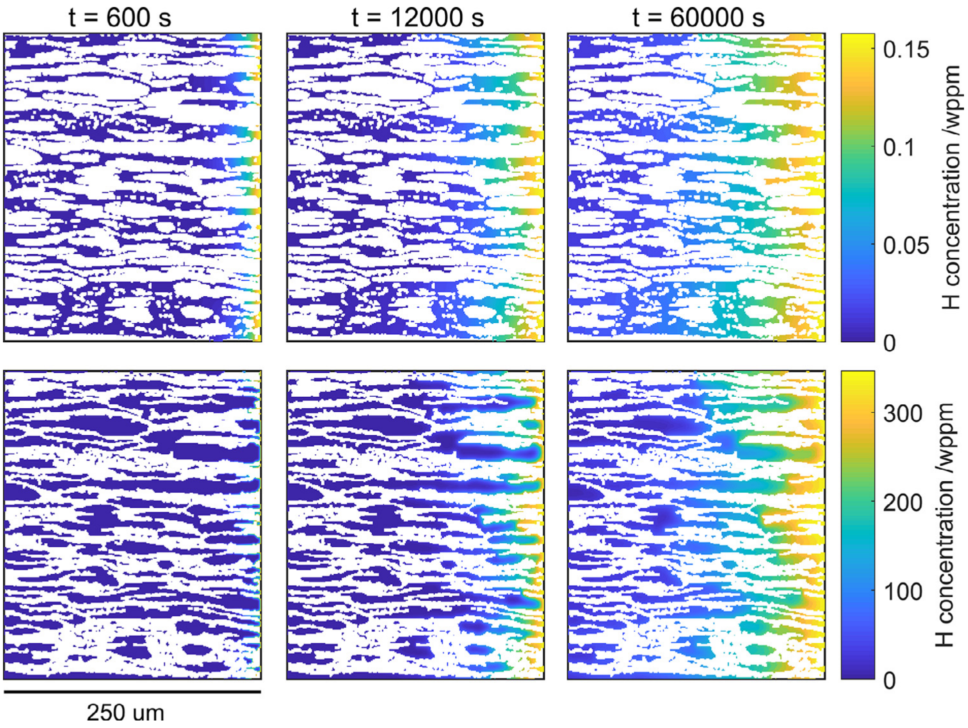

Fig. 9. Maps of H concentration in ferrite (top row) and austenite (bottom row) in the simulated ROL sample at different times. Diffusion direction is from right to left.

decreases the rate of diffusion in ferrite dramatically. This demonstrates that treating H diffusion in ferrite and in austenite independently, as in some previous studies [23,24], is an oversimplification of the problem.

The results also show that the simulated H absorption rates overestimate experimental data, particularly for short charging times and for the ROL sample, as illustrated in Fig. 10. Given that the values of lattice diffusivity in ferrite and austenite are known to be close to the values used here and that trapping effects are unlikely to play a significant role as discussed later, the most probable cause for this is that the kinetics of H absorption into austenite are in fact much slower than those resulting from Eq. (5). To examine the effect of absorption kinetics, H diffusion into a small 5 µm rectangular domain of austenite embedded in a ferrite matrix was simulated. As in the simulations above, the boundary conditions were set to zero-flux on three of the edges while on one

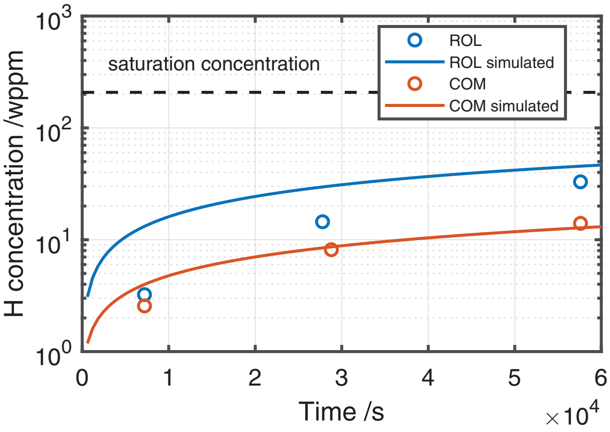

Fig. 10. Experimental and simulated absorbed H concentration as a function of charging time in the two types of samples using the ferrite-austenite interface condition from Eq. (5). Diffusion direction is from right to left.

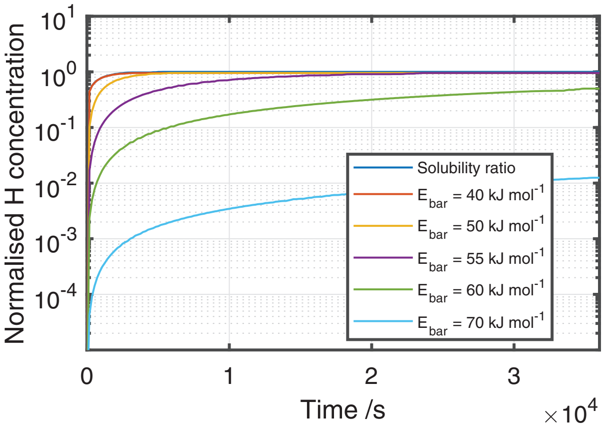

Fig. 11. Effect of different boundary conditions at the ferrite-austenite interface. Solubility ratio refers to Eq. (5) while E_{bar} values refer to Eq. (4) and includes the effect of an energy barrier at the interface. The latter produces slower saturation kinetics, although the difference only becomes apparent for E_{bar} values exceeding 50 kJ mol^{-1}.

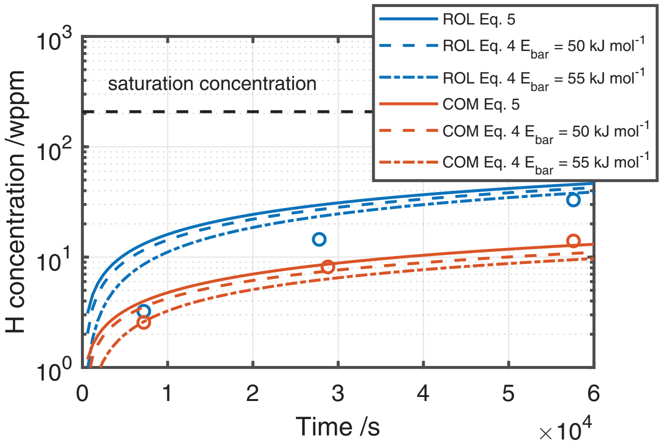

Fig. 12. Simulated absorbed H concentration as a function of charging time in the two types of samples. The results produced by the ferrite-austenite interface condition from Eq. (5) are compared to those from Eq. (4). The latter leads to better correspondence with the experimental data shown as circles.

of them a constant-concentration boundary condition was applied. The results shown in Fig. 11 demonstrate that applying Eq. (4) can indeed result in much slower H absorption compared to Eq. (5). The difference only becomes significant, however, when E_{bar} exceeds about 50 kJ mol^{-1}.

To see whether a better agreement to experimental data could be obtained, another set of simulations was run using Eq. (4) to define the flux at the ferrite-austenite interface with E_{bar} values of 50 kJ mol^{-1} and 55 kJ mol^{-1}. The results are shown in Fig. 12 and exhibit a better agreement to experimental data, particularly at shorter diffusion times. This indicates that there is likely an energy barrier associated to the transition of H from the ferrite matrix into the islands of austenite. The model begins to underpredict the absorption rate for the COM samples and that the simulated difference in the absorption rates between COM and ROL samples is larger than the experiments suggest. This will be discussed later.

The initial overprediction of the absorption rate from the model may also be related to transient effects related to subsurface phenomena. If that is the case, the boundary conditions need to be time-dependent and calibrated accordingly. However, not much literature relevant to the particular case of H generation on the surface of iron in an aqueous solution was found and thus boundary conditions during charging were assumed to be constant. Nonetheless, there are several possible complicating factors that might make the boundary conditions time-dependent: (1) The presence of an interface chromia layer during H charging. Only one study was found attempting to quantify this effect [58]. The authors found that due to its slow H diffusion coefficient, an oxide layer can act as a permeation barrier. However, this effect was not quantified with sufficient accuracy as to be used in our study. Assuming the chromia layer remains constant, its presence is already implicitly taken into account with the experimentally determined boundary condition. If however, the layer dissolves during charging, it may result in a gradual increase in the adsorption rate up until it is completely reduced. This could explain the discrepancy between the model and the experiment for short charging times. However, further work would be required to quantify the kinetics of the oxide layer formation/dissolution in duplex steels and understand the solubility and diffusivity of H in the layer to predict this effect. (2) Some literature suggests austenitic steels may develop a thin hydride layer during cathodic H charging [59], which would imply that H absorption is initially accelerated due to the formation of hydrides. Subsequently, these hydrides may act as obstacles, limiting the rate of H accumulation in the sample. Hydride formation therefore cannot provide an explanation for the discrepancy. Regardless, in a duplex steel, this mechanism would likely apply to a lesser degree since to the authors knowledge, there is no experimental evidence of hydrides forming in ferrite. (3) Austenite grains in a similar duplex steel have been shown to undergo a partial martensitic transformation during charging [60]. It might be possible that this increases the absorption rate due to the generation of defects in austenite. Again, however, this would imply that the experimental absorption rate should be faster than the model suggests and does not explain the discrepancy. In any case, the presence of surface damage in our samples was unlikely. In a previous study on the same steel a similar solution but a much higher current density were used for H charging. No surface damage was observed [22]. (4) The kinetics of H absorption slow down over time due to electrochemical processes, perhaps a slight change in the composition of the charging solution or the surface of the metal. That would imply that the constant-concentration boundary condition used in the simulations is inaccurate and that it would actually need to be a decreasing function of time. In future work, this assumption could be verified by performing a permeation experiment using the same charging conditions as in the manuscript. Currently, however, there are no relevant studies available. In sum-

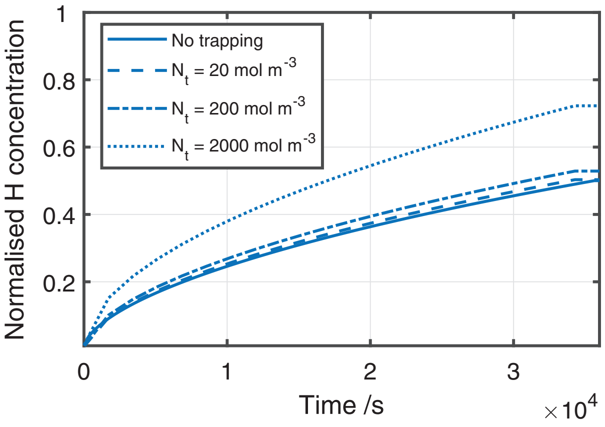

Fig. 13. Total H absorption rate in duplex steel as a function of trap density in ferrite. The rate increases with density, indicating that any potential decrease on the rate of absorption of H into austenite islands is more than offset by the increase of H absorbed by traps in ferrite.

mary, surface phenomena are complex and it is likely that had an impact on the experimental results that was not considered in our model. More experimental analysis is required to better understand the rate-controlling effects at the surface so they can be incorporated into the model. This is an important topic that has not been sufficiently elucidated and a crucial component in a better understanding of H diffusion and embrittlement.

5.3.1. Effect of trapping in ferrite

We also tested the effect of traps on the H absorption rate using the interface boundary conditions from Eq. (5) to see whether they can appreciably reduce it. To ensure significant trapping in ferrite, a relatively high binding energy ΔE_t of 45 kJ mol^{-1} was chosen. Trap-free austenite was assumed as it was expected that trapping in ferrite would be the key factor in decreasing the absorption rate. Several simulations were ran on the ROL microstructure exploring the effect of trap density. The results are displayed in Fig. 13 and show that traps actually increase the H absorption rate. This can be understood in the following way: despite the fact that trapping decreases the effective diffusivity in ferrite, the decrease is not significant enough to affect the H absorption rate into austenite considerably. While the latter is somewhat decreased, the additional H bound to traps in ferrite is more than enough to offset this decrease. H trapped in ferrite becomes a significant fraction of the total H in the sample at high N_t values. Very similar results were obtained when the same trapping parameters were applied to both ferrite and austenite.

These results are in line with the observations in part I where the initial insight from modelling was that a higher trap density always results in a larger H absorption rate due to the contribution of trapped H, despite the fact that the effective diffusivity of H decreases. Simply put, the flux of H being funneled into traps is always larger than the flux of H towards the centre of the sample, in agreement with the local equilibrium condition. Furthermore, since the density of dislocations in hot-rolled duplex steels has been shown to be low [9] and other defects (grain boundaries, vacancies and carbides) were either relatively sparse or completely absent, trapping effects are unlikely to play an important role in duplex steel.

5.3.2. Thermal desorption analysis: modelling and experiments

To correlate H absorption to austenite orientation, further analysis was done on the thermal desorption data. Fig. 14 shows the experimental desorption curves for (a) COM and (b) ROL for different charging times, 2 h, 8 h and 16 h; the area under each curve corresponds to the total concentration estimated in Figs. 10 and 12. There are two peaks in both conditions, one between 75 °C and 100 °C and another one around 270 °C. The height of the peaks in ROL samples was systematically higher than their counterparts for COM samples (note the limits in the y axis are different), consistent with more H being measured in the ROL samples (Fig. 10). In COM samples, the temperature of the first peak increases with increasing charging time, while the second peak stays nearly constant. As for ROL samples, the second peak seems to increase at a similar rate as the first one. In addition, the second peak in COM samples seems more pronounced than in ROL, *e.g.* the height of both peaks after 2h of charging is very similar but then seems to saturate for longer charging times. The second peak in the ROL samples is possibly shifted to lower temperatures, but since only a slight shoulder is visible it is difficult to determine its exact location, although it seems ~30 °C lower than the one in COM samples.

TDA simulations of the microstructures charged for 16 h were conducted to understand the origin of the peaks observed experimentally. The initial concentration was that from the previous charging simulation, followed by a 600 s desorption at 300 K, using Eq. (6) for the conditions at the ferrite-austenite interface. All the model parameters were kept the same except for D_α, which was missing temperature dependence. To rectify this, the activation energy was assumed to be the same as in pure ferrite (3.85 kJ mol^{-1} [61]) and the prefactor was rescaled to match 3.87×10^{-10} m^2 s^{-1} (used previously) at 300 K. The predicted desorption curves are shown in full lines in Fig. 14c and the corresponding concentration distribution in the COM sample is shown in Fig. 15; the ferrite-austenite interface conditions were from Eq. (5). The model successfully predicts the occurrence of the two peaks, where the second peak is due to back diffusion (discussed below), and in the COM sample it also captures the height of the peaks. However, the height and location of the first peak for ROL sample is much lower than experimentally observed, whereas the second peak is predicted to be more pronounced and shifted to higher temperatures. This discrepancy is likely due to the barrier effect at the ferrite-austenite interface since further TDA simulation results using a barrier energy of 55 kJ mol^{-1} (Fig. 14c, dashed lines) show an appreciably better correlation to the experimental data for the ROL case, and an equally good one for the COM case. This further corroborates the conclusion about the presence of a diffusion barrier energy at the ferrite-austenite interface. In the case of the ROL sample, the barrier energy reduces the H flux from austenite to ferrite at low temperatures, meaning most H is retained in the austenite near the surface. This decreases the back diffusion effect, producing an earlier onset of the second peak. For the COM sample, the austenite morphology itself prevents excessive back diffusion even when no interface barrier energy is present therefore the two desorption curves appear quite similar. Other reasons for the discrepancies are the same discussed in the previous sections.

The H distribution in the COM samples (Fig. 15) shows that most H is located at the surface near the location of the first peak (99 °C) which can diffuse out as the temperature increases, while a part continues diffusing to the centre (seen at 200 °C). At 350 °C, the remaining H is in the centre of the sample (left-hand side). The back diffusion effect is consistent with findings in single-phase FCC alloys where H is concentrated near the surface after charging. For instance, we reported the back diffusion effect in previous studies on GB trapping in Fe-Ni FCC alloys [39] and on H diffusion in an austenitic steel [62]. The same finding was reported by Claeys et al. [31] studying thermal desorption of duplex steel. Samples that were not saturated with H showed two distinct peaks, the second one due to back diffusion, and a only single peak for fully saturated samples.

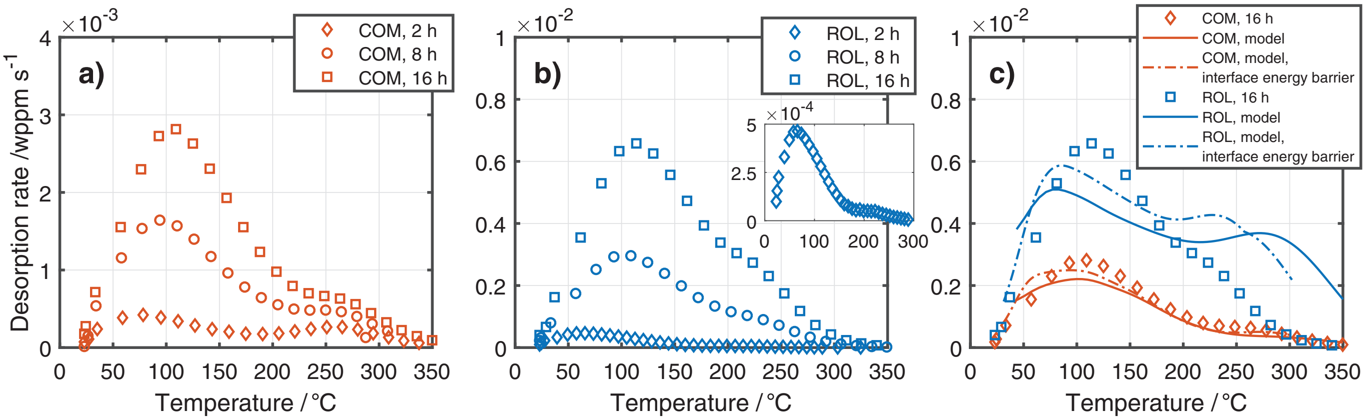

Fig. 14. Thermal desorption curves for (a) COM and (b) ROL samples for different charging times. (c) Predicted permeation curves in COM and ROL for 16h charging conditions.

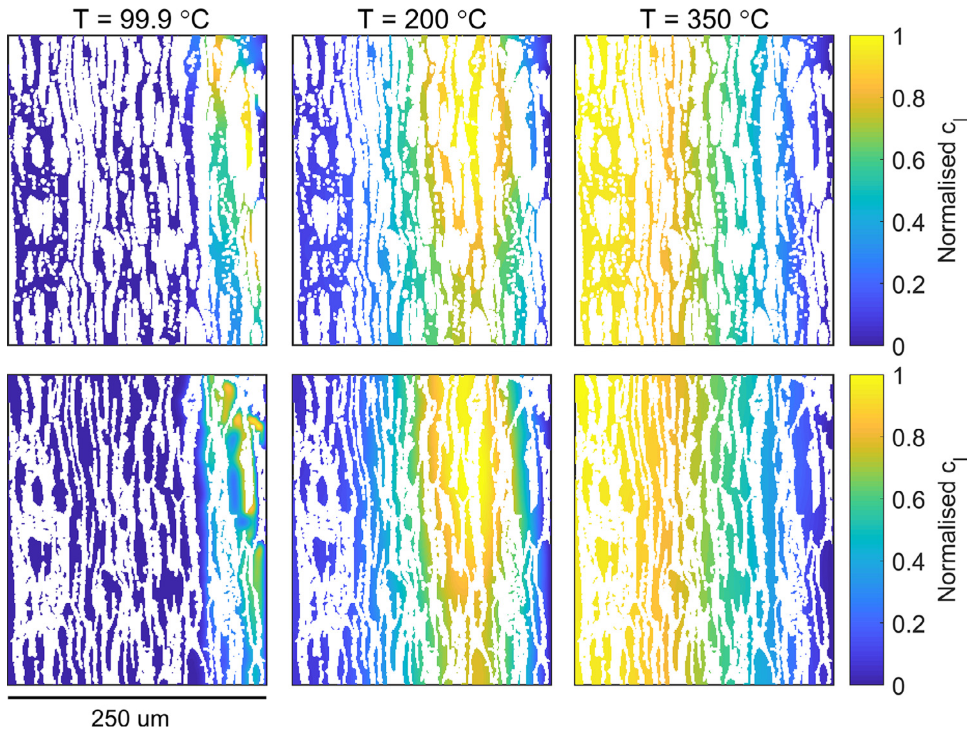

Fig. 15. Maps of normalised H concentration in ferrite (top row) and austenite (bottom row) in the simulated COM sample at different desorption temperatures. Diffusion direction is from right to left. Concentration is normalised relative to the maximum value in the domain at every temperature to better illustrate H distribution.

5.3.3. Discussion

The study of H absorption rate on the duplex samples again highlights the importance of austenite morphology but also reveals some unexpected behaviour. In the simulated COM sample, with austenite plates normal to the H diffusion direction, the absorption rate was expected to significantly underestimate the experimentally measured values. This is because in our 2D simulations, the austenite grains were effectively infinitely long normal to the input microstructure. In reality, and as apparent from Fig. 1b, that dimension may in fact be fairly small, providing a short diffusion pathway. Despite this, the simulated absorption rate was equal to or slightly lower than measured. It was shown that trapping effects cannot explain this since they only further increase the absorption rate. It is also unlikely to be due to our underestimating of the lattice diffusion coefficients in ferrite and austenite, which are at the very bottom end of values reported for ferrite and austenite [52]. Instead, the most plausible explanation seems to be that an energy barrier is associated to the H transition from ferrite to austenite, which decreases the overall rate of H absorption. However, in the COM sample, with austenite plates normal to the H diffusion direction, the potential decrease in absorption rate due to an energy barrier is difficult to deconvolve from the decrease due to the aforementioned missing dimension. It is instead more instructive to look at the ROL samples where austenite plates are parallel to the H diffusion direction. There, adding an extra dimension would not add a short diffusion pathway. The absorption kinetics would therefore be expected to stay the same and so the simulations on ROL input masks are expected to be more representative of the real behaviour. However, the simulation results on ROL masks indicate that only using the boundary condition from Eq. (4) with a relatively high energy barrier E_{bar} yields the absorption rates somewhat in line with the experiments.

This value is much larger than what would be expected based on an idealised H potential landscape at the interface shown in

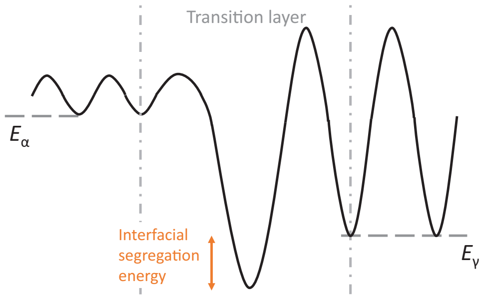

Fig. 16. Proposed energy landscape at the α-γ interface with an associated interfacial segregation energy which slows down the diffusion of H atoms from one phase to the other.

Fig. 3, which should be at most some 35 kJ mol^{-1} (the difference between the activation energy for H diffusion in austenite and the energy difference between ferrite and austenite). What seems more likely is that there is some additional segregation energy relative to the austenite phase at the very interface. This scenario is illustrated in Fig. 16, in which the orange arrows denote this additional interface segregation energy, which could also be related to the lattice misfit or the presence of dislocations at the interface. The result is a somewhat more complicated interface for which the bilayer model (Eq. (4)) is not, strictly speaking, valid, as there are now three, rather than two, distinct H sites in the transition layer. Regardless, the H potential landscape near the ferrite-austenite interface has not been studied to date so the bilayer model offers a first approximation. The height of the energy barrier is unknown as no first-principles computational studies have tackled this problem yet. Fitting the barrier to match the experimentally measured absorption rate in the ROL direction using the approach presented here, yields only a rough estimate. It could, however, be further improved by extending the simulations to three dimensions and using a somewhat larger simulation domain to capture the effect of austenite morphology more accurately.

Thermal desorption analysis showed that two peaks are present in duplex steels, irrespective of the orientation of the austenite islands. The model showed that the first peak is due to H close to the surface which is able to the leave sample relatively easily, whereas the second peak is a result of back diffusion and not strong point traps as it is sometimes assumed. The second peak is a result of H making its way to the centre of the sample during heating, which requires a further increase in temperature for complete desorption. This phenomenon has also been observed in single-phase FCC alloys where most H was concentrated near the surface before the thermal desorption experiment.

This work paves the way towards predicting how austenite affects hydrogen diffusion in steels, although further work is needed to expand the model to 3D in order to capture features such as phase connectivity more accurately, in addition to accounting for possible surface–related effects. For instance, previous experimental findings have postulated that the effect of retained austenite in ferritic microstructures can be opposing, depending on its volume fraction [63]: hydrogen absorption is low if the austenite fraction is high enough for the austenite grains to be fully interconnected, whereas high H absorption occurs if the austenite fraction is lower than some critical value (the percolation threshold) as austenite islands are disconnected, and unable to ‘block’ the diffusing hydrogen. However, the value of the percolation threshold volume fraction depends on the morphology of austenite, and our model demonstrates that clearly for the first time. We touch upon the problem of percolation by showing how two microstructures (*e.g.* ROL and COM) exhibit very different H absorption rates despite having the same volume fraction of austenite. In future studies, the model could also be applied to study the effect of austenite volume fraction on the absorption rate in duplex steels and to determine the exact value of the percolation threshold for this microstructure. The extension to 3D is in fact fairly straightforward, although the current implementation is somewhat constrained by the numerical scheme. It is expected that implementing it as an implicit or implicit-explicit finite difference scheme or as a finite element scheme in a commercial package such as Abaqus would rectify the long calculation times resulting from the constraint on the size of the time step. This would allow one to treat more finely discretised microstructures, opening up the possibility of simulating H diffusion in other austenite-containing alloys such as TRIP, quenched-and-partitioned and superbainitic steels. Coupled with techniques such as serial sectioning or X-ray tomography, it would be of particular interest to examine the effect of real, three-dimensional austenite morphology on H diffusion.

6. Conclusions

The aim of this work was to better account for the effect of austenite on H diffusion in ferritic-austenitic steels by foregoing the point trap approximation sometimes used to model its effect. It was instead accounted for explicitly by treating it in two dimensions as a domain with a different H lattice diffusivity and solubility. In summary:

- The modelling results showed that in the presence of a secondary phase in which bulk trapping is possible, the local equilibrium approximation for trapping is insufficient as it does not accurately represent the diffusion kinetics, which become heavily dependent on the morphology of this phase and the conditions at the ferrite-austenite interface for which a deeper understanding at the atomic level is needed. This is not only applicable to steels but also to other alloys containing two or more phases with different H solubilities, for example titanium alloys. Our modelling results also helped confirm some experimentally observed phenomena, such as the percolation effect in austenitic-ferritic microstructures.
- The simulated permeation transients show that the presence of austenite can strongly decrease the steady-state flux as well as the effective diffusivity when austenite grains are elongated and lie normal to the direction of diffusion. The decrease in effective diffusivity is more pronounced than the decrease in steady-state flux, which can partly explain the steep rise in permeation transients due to the presence of retained austenite in the samples studied in part I of this series. However, quench vacancies are likely factors as well.
- In duplex steels the rate of H absorption and the effective diffusivity are both sensitive to austenite morphology – both are significantly lower when austenite grains are elongated and oriented normal to the diffusion direction, which is in line with earlier experimental findings. Thermal desorption analysis showed two H peaks, irrespective of the orientation of the austenite islands. The first peak was due to H concentrated close to the surface diffusing out, whereas the second peak was due to back diffusion.
- Based on a comparison between the simulations and experimental data it was concluded that an energy barrier associated to the H transition from ferrite to austenite is necessary to capture the overall rate of H absorption. Modelling diffusion without accounting for the barrier results in absorption rates much higher than experimentally observed.

We showed in this two-part series that combining thorough experimental characterisation with modelling is effective at deconvolving the impact of various microstructural features on H diffusion in multiphase steels. This was critical in part I in highlighting the strong influence retained austenite films have on the effective H diffusivity in martensite; similarly, we were able to show the combined effects of H trapping on dislocations and grain boundaries in fine-grained microstructures such as martensite and heavily deformed ferrite. In part II, when H diffusion in austenite and kinetics at ferrite-austenite interfaces were considered in duplex steels, it was possible to demonstrate the effect of austenite plates impeding H diffusion when they lie normal to the diffusion direction. Such processes would not have been possible to elucidate if austenite were considered as a point trap under the local equilibrium assumption.

Declaration of Competing Interest

None.

Acknowledgments

We gratefully acknowledge the funding received from the HEmS project (grant number EP/L014742/1) and the EPSRC-Rolls Royce strategic partnership (EPSRC grant numbers EP/H022309/1 and EP/H500375/1). E. I. Galindo-Nava acknowledges the Royal Academy of Engineering for his research fellowship funding and A. Turk would like to thank Steve Ooi for assistance with experimental work.

References

[1] J.H. Ryu, Hydrogen Embrittlement in TRIP and TWIP Steels, Pohang, South Korea: Pohang University of Science and Technology, 2012 Ph.D. thesis.

[2] M. Koyama, S. Okazaki, T. Sawaguchi, K. Tsuzaki, Hydrogen Embrittlement Susceptibility of Fe-Mn Binary Alloys with High Mn Content: Effects of Stable and Metastable ϵ-Martensite, and Mn Concentration, Metallurg. Mater. Trans. A 47 (6) (2016) 2656–2673, doi:10.1007/s11661-016-3431-9.

[3] J. Yang, F. Huang, Z. Guo, Y. Rong, N. Chen, Effect of retained austenite on the hydrogen embrittlement of a medium carbon quenching and partitioning steel with refined microstructure, Mater. Sci. Eng. A 665 (2016) 76–85, doi:10.1016/j.msea.2016.04.025.

[4] S.L.I. Chan, H.L. Lee, J.R. Yang, Effect of retained austenite on the hydrogen content and effective diffusivity of martensitic structure, Metallurg. Trans. A 22 (11) (1991) 2579–2586, doi:10.1007/BF02851351.

[5] D. Pérez Escobar, K. Verbeken, L. Duprez, M. Verhaege, Evaluation of hydrogen trapping in high strength steels by thermal desorption spectroscopy, Mater. Sci. Eng. A 551 (2012) 50–58, doi:10.1016/j.msea.2012.04.078.

[6] D. Pérez Escobar, T. Depover, L. Duprez, K. Verbeken, M. Verhaege, Combined thermal desorption spectroscopy, differential scanning calorimetry, scanning electron microscopy and X-ray diffraction study of hydrogen trapping in cold deformed TRIP steel, Acta Mater. 60 (6) (2012) 2593–2605, doi:10.1016/j.actamat.2012.01.026.

[7] F. Iacoviello, M. Habashi, M. Cavallini, Hydrogen embrittlement in the duplex stainless steel Z2CND2205 hydrogen-charged at 200 C, Mater. Sci. Eng. A 224 (1) (1997) 116–124, doi:10.1016/S0921-5093(96)10545-1.

[8] G. Martin, Hot workability of duplex stainless steels, Université de Grenoble, Grenoble, 2011 Ph.D. thesis.

[9] X.Z. Liang, M.F. Dodge, S. Kabra, J.F. Kelleher, T.L. Lee, H.B. Dong, Effect of hydrogen charging on dislocation multiplication in pre-strained super duplex stainless steel, Scripta Mater. 143 (2018) 20–24, doi:10.1016/j.scriptamat.2017.09.001.

[10] A. Turnbull, R.B. Hutchings, Analysis of hydrogen atom transport in a two-phase alloy, Mater. Sci. Eng. A 177 (1) (1994) 161–171, doi:10.1016/0921-5093(94)90488-X.

[11] R. Silverstein, D. Eliezer, Mechanisms of hydrogen trapping in austenitic, duplex, and super martensitic stainless steels, J. Alloys Comp. 720 (2017) 451–459, doi:10.1016/j.jallcom.2017.05.286.

[12] E. Dabah, T. Kannengiesser, T. Mente, K. Beyer, S. Brauser, Quantification of hydrogen effective diffusion coefficients and effusion behavior in duplex stainless steel weld metals, Welding World 57 (4) (2013) 561–567, doi:10.1007/s40194-013-0051-5.

[13] L. Claeys, T. Depover, I. DeGraeve, K. Verbeken, Electrochemical hydrogen charging of duplex stainless steel, Corrosion (2018), doi:10.5006/2959.

[14] W.C. Luu, P.W. Liu, J.K. Wu, Hydrogen transport and degradation of a commercial duplex stainless steel, Corros. Sci. 44 (8) (2002) 1783–1791 https://doi.org/10.1016/S0010-938X(01)00143-3.

[15] B.R.S. Da Silva, F. Salvio, D.S. Dos Santos, Hydrogen Embrittlement in Super Duplex Stainless Steel Tubes UNS S32750 Under Mechanical Stress, in: Proceedings of the International Hydrogen Conference, Jackson, WY, 2012, pp. 09–12.

[16] T. Tanaka, K. Kawakami, S.-i. Hayashi, Visualization of deuterium flux and grain boundary diffusion in duplex stainless steel and Fe–30 % Ni alloy, using secondary ion mass spectrometry equipped with a Ga focused ion beam, J. Mater. Sci. 49 (11) (2014) 3928–3935, doi:10.1007/s10853-013-7956-7.

[17] R. Silverstein, D. Eliezer, Hydrogen trapping mechanism of different duplex stainless steels alloys, J. Alloys Compou. 644 (2015) 280–286, doi:10.1016/j.jallcom.2015.04.176.

[18] S.S. Chen, T.I. Wu, J.K. Wu, Effects of deformation on hydrogen degradation in a duplex stainless steel, J. Mater. Sci. 39 (1) (2004) 67–71, doi:10.1023/B:JMSC.0000007729.14528.a8.

[19] R. Kaçar, Effect of solidification mode and morphology of microstructure on the hydrogen content of duplex stainless steel weld metal, Mater. Des. 25 (1) (2004) 1–9, doi:10.1016/S0261-3069(03)00169-9.

[20] S. Brauser, T. Kannengiesser, Hydrogen absorption of different welded duplex steels, Int. J. Hydrogen Energy 35 (9) (2010) 4368–4374, doi:10.1016/j.ijhydene.2010.01.148.

[21] H.K. Yalçì, D.V. Edmonds, Application of the hydrogen microprint and the microautoradiography techniques to a duplex stainless steel, Mater. Character. 34 (2) (1995) 97–104, doi:10.1016/1044-5803(94)00056-Q.

[22] S. Pu, Hydrogen in Austenite: What Changes after Martensitic Transformation?, University of Cambridge, 2019 Thesis. doi: 10.17863/CAM.41647

[23] E. Owczarek, T. Zakroczymski, Hydrogen transport in a duplex stainless steel, Acta Mater. 48 (12) (2000) 3059–3070.

[24] T. Zakroczymski, E. Owczarek, Electrochemical investigation of hydrogen absorption in a duplex stainless steel, Acta Mater. 50 (10) (2002) 2701–2713, doi:10.1016/S1359-6454(02)00105-2.

[25] T. Mente, T. Bollinghaus, Modeling Of Hydrogen Distribution in a Duplex Stainless Steel, Weld. World 56 (11-12) (2012) 66–78, doi:10.1007/BF03321397.

[26] J. Yao, D.D. Macdonald, M. Macdonald, F. Cao, C. Dong, Hydrogen permeation in 2205 duplex stainless steel under hydrostatic pressure and simulation by COMSOL, Mater. Corros. (2018), doi:10.1002/maco.201810552.

[27] V. Olden, A. Saai, L. Jemblie, R. Johnsen, FE simulation of hydrogen diffusion in duplex stainless steel, International Journal of Hydrogen Energy 39 (2) (2014) 1156–1163, doi:10.1016/j.ijhydene.2013.10.101.

[28] M. Enomoto, Simulation of thermal desorption spectrum of hydrogen from austenite embedded in the martensite matrix, International Journal of Hydrogen Energy (2017), doi:10.1016/j.ijhydene.2017.01.199.

[29] Y. Shibamoto, Y. Mikami, M. Mochizuki, Modeling of Hydrogen Diffusion Behavior Considering the Microstructure of Duplex Stainless Steel Weld Metal, Q. J. Jpn Welding Soc. 35 (2) (2017) 23–27.

[30] E. Tohme, V. Barnier, F. Christien, C. Bosch, K. Wolski, M. Zamanzade, SKPFM study of hydrogen in a two phase material. Experiments and modelling, Int. J. Hydrogen Energy 44 (33) (2019) 18597–18605, doi:10.1016/j.ijhydene.2019.05.177.

[31] L. Claeys, V. Cnockaert, T. Depover, I. De Graeve, K. Verbeken, Critical assessment of the evaluation of thermal desorption spectroscopy data for duplex stainless steels: A combined experimental and numerical approach, Acta Mater. 186 (2020) 190–198, doi:10.1016/j.actamat.2019.12.055.

[32] M.J. Peet, T. Hojo, Hydrogen Susceptibility of Nanostructured Bainitic Steels, Metallurg. Mater. Trans. A 47 (2) (2016) 718–725, doi:10.1007/s11661-015-3221-9.

[33] K. Kawakami, T. Matsumiya, Numerical analysis of hydrogen trap state by TiC and V4C3 in BCC-Fe, ISIJ Int. 52 (9) (2012) 1693–1697, doi:10.2355/isijinternational.52.1693.

[34] E.J. McEniry, T. Hickel, J. Neugebauer, Ab initio simulation of hydrogen-induced decohesion in cementite-containing microstructures, Acta Mater. 150 (2018) 53–58, doi:10.1016/j.actamat.2018.03.005.

[35] D. Di Stefano, R. Nazarov, T. Hickel, J. Neugebauer, M. Mrovec, C. Elsässer, First-principles investigation of hydrogen interaction with TiC precipitates in α-Fe, Phys. Rev. B 93 (18) (2016) 184108, doi:10.1103/PhysRevB.93.184108.

[36] Y.D. Park, I.S. Maroef, A. Landau, D.L. Olson, Retained Austenite as a Hydrogen Trap in Steel Welds, Welding J. 81 (2002) 27S–35S.

[37] D. Di Stefano, M. Mrovec, C. Elsässer, First-principles investigation of hydrogen trapping and diffusion at grain boundaries in nickel, Acta Mater. 98 (2015) 306–312, doi:10.1016/j.actamat.2015.07.031.

[38] A. Turk, D. San Martín, P.E.J. Rivera-Díaz-del-Castillo, E.I. Galindo-Nava, Correlation between vanadium carbide size and hydrogen trapping in ferritic steel, Scripta Mater. 152 (2018) 112–116, doi:10.1016/j.scriptamat.2018.04.013.

[39] A. Turk, D. Bombač, J. Jelita Rydel, M. Ziętara, P.E.J. Rivera-Díaz-del-Castillo, E.I. Galindo-Nava, Grain boundary carbides as hydrogen diffusion barrier in a Fe-Ni alloy: A thermal desorption and modelling study, Mater. Des. 160 (2018) 985–998, doi:10.1016/j.matdes.2018.10.012.

[40] Abaqus 6.14 Documentation, ????, (http://abaqus.software.polimi.it/v6.14/index.html).

[41] J. Toribio, V. Kharin, A generalised model of hydrogen diffusion in metals with multiple trap types, Philosoph. Mag. 95 (31) (2015) 3429–3451, doi:10.1080/14786435.2015.1079660.

[42] J. Leblond, D. Dubois, A general mathematical description of hydrogen diffusion in steels—I. Derivation of diffusion equations from Boltzmann-type transport equations, Acta Metall. 31 (10) (1983) 1459–1469, doi:10.1016/0001-6160(83)90142-6.

[43] D.N. Ilin, Simulation of Hydrogen Diffusion in FCC Polycrystals. Effect of Deformation and Grain Boundaries: Effect of Deformation and Grain Boundaries, Universite de Bordeaux, Bordeaux, 2014 Ph.D. thesis.

[44] S. Hofmann, J. Erlewein, A model of the kinetics and equilibria of surface segregation in the monolayer regime, Surface Sci. 77 (3) (1978) 591–602, doi:10.1016/0039-6028(78)90143-7.

[45] Y.A. Du, L. Ismer, J. Rogal, T. Hickel, J. Neugebauer, R. Drautz, First-principles study on the interaction of H interstitials with grain boundaries in α- and γ-Fe, Phys. Rev. B 84 (14) (2011) 144121, doi:10.1103/PhysRevB.84.144121.

[46] R.A. Oriani, The diffusion and trapping of hydrogen in steel, Acta Metall. 18 (1) (1970) 147–157, doi:10.1016/0001-6160(70)90078-7.

[47] J. Crank, The Mathematics of Diffusion, 2d ed, Clarendon Press, Oxford, [Eng], 1975.

[48] T.-P. Perng, C. Altstetter, Effects of deformation on hydrogen permeation in austenitic stainless steels, Acta Metall. 34 (9) (1986) 1771–1781.

[49] C.H. Tseng, W.Y. Wei, J.K. Wu, Electrochemical methods for studying hydrogen diffusivity, permeability, and solubility in AISI 420 and AISI 430 stainless steels, Mater. Sci. Technol. 5 (12) (1989) 1236–1239, doi:10.1179/mst.1989.5.12.1236.

[50] R. Gangloff, B. Somerday, Gaseous Hydrogen Embrittlement of Materials in Energy Technologies: The Problem, Its Characterisation and Effects on Particular Alloy Classes, n v. 1, Woodhead Publishing Series in Metals and Surface Engineering, Elsevier Science, 2012.

[51] K. Kiuchi, R.B. McLellan, The solubility and diffusivity of hydrogen in well-annealed and deformed iron, Acta Metall. 31 (7) (1983) 961–984 https://doi.org/10.1016/0001-6160(83)90192-X.

[52] C. San Marchi, B.P. Somerday, S.L. Robinson, Permeability, solubility and diffusivity of hydrogen isotopes in stainless steels at high gas pressures, Int. J. Hydrogen Energy 32 (1) (2007) 100–116 https://doi.org/10.1016/j.ijhydene.2006.05.008.

[53] F.D. Fischer, J. Svoboda, E. Kozeschnik, Interstitial diffusion in systems with multiple sorts of traps, Model. Simul. Mater. Sci. Eng. 21 (2) (2013) 025008, doi:10.1088/0965-0393/21/2/025008.

[54] M.A.V. Devanathan, Z. Stachurski, The Adsorption and Diffusion of Electrolytic Hydrogen in Palladium, Proc. R. Soc. Lond. A Math. Phys. Eng. Sci. 270 (1340) (1962) 90–102, doi:10.1098/rspa.1962.0205.

[55] J.L. Auriault, Heterogeneous medium. Is an equivalent macroscopic description possible? Int. J. Eng. Sci. 29 (7) (1991) 785–795, doi:10.1016/0020-7225(91)90001-J.

[56] S.J. Kim, D.W. Yun, D.W. Suh, K.Y. Kim, Electrochemical hydrogen permeation measurement through TRIP steel under loading condition of phase transition, Electrochem. Commun. 24 (2012) 112–115, doi:10.1016/j.elecom.2012.09.002.

[57] L. Lan, X. Kong, Z. Hu, C. Qiu, D. Zhao, L. Du, Hydrogen permeation behavior in relation to microstructural evolution of low carbon bainitic steel weldments, Corros. Sci. 112 (2016) 180–193, doi:10.1016/j.corsci.2016.07.025.

[58] E. Legrand, J. Bouhattate, X. Feaugas, H. Garmestani, Computational analysis of geometrical factors affecting experimental data extracted from hydrogen permeation tests: II - Consequences of trapping and an oxide layer, Int. J. Hydrogen Energy 37 (18) (2012) 13574–13582 https://doi.org/10.1016/j.ijhydene.2012.06.043. ICCE-2011.

[59] A. Szummer, A. Janko, Hydride Phases in Austenitic Stainless Steels, CORROSION 35 (10) (1979) 461–464, doi:10.5006/0010-9312-35.10.461.

[60] A. Głowacka, M. Woźniak, G. Nolze, W. Świątnicki, Hydrogen induced phase transformations in austenitic-Ferritic Steel, Solid State Phenomena 112 (2006) 133–140, doi:10.4028/www.scientific.net/SSP.112.133.

[61] M. Nagano, Y. Hayashi, N. Ohtani, M. Isshiki, K. Igaki, Hydrogen diffusivity in high purity alpha iron, Scripta Metallur. 16 (8) (1982) 973–976, doi:10.1016/0036-9748(82)90136-3.

[62] S. Pu, A. Turk, S. Lenka, S. Ooi, Study of hydrogen release resulting from the transformation of austenite into martensite, Mater. Sci. Eng. A 754 (2019) 628–635, doi:10.1016/j.msea.2019.03.098.

[63] L.C.D. Fielding, E.J. Song, D.K. Han, H.K.D.H. Bhadeshia, D.-W. Suh, Hydrogen diffusion and the percolation of austenite in nanostructured bainitic steel, Proc. R. Soc. Lond. A Math. Phys. Eng. Sci. 470 (2168) (2014) 20140108, doi:10.1098/rspa.2014.0108.